

# Two-Body T-Matrices without Angular Momentum Decomposition: Energy and Momentum Dependencies

Ch. Elster, J.H. Thomas

*Institute of Nuclear and Particle Physics, and Department of Physics,  
Ohio University, Athens, OH 45701*

W. Glöckle

*Institute for Theoretical Physics II, Ruhr-University Bochum, D-44780 Bochum, Germany.*  
(August 22, 2019)

## Abstract

The two-body t-matrix is calculated directly as function of two vector momenta for different Malfliet-Tjon type potentials. At a few hundred MeV projectile energy the total amplitude is quite a smooth function showing only a strong peak in forward direction. In contrast the corresponding partial wave contributions, whose number increases with increasing energy, become more and more oscillatory with increasing energy. The angular and momentum dependence of the full amplitude is studied and displayed on as well as off the energy shell as function of positive and negative energies. The behavior of the t-matrix in the vicinity of bound state poles and resonance poles in the second energy sheet is studied. It is found that the angular dependence of T exhibits a very characteristic behavior in the vicinity of those poles, which is given by the Legendre function corresponding to the quantum number either of the bound state or the resonance (or virtual) state. This behavior is illustrated with numerical examples.

## I. INTRODUCTION

At low energies in the MeV and the few tenth of MeV region very few angular momenta contribute to the nucleon-nucleon (NN) scattering process. Consequently a description using angular momentum decomposition is an adequate tool for carrying out scattering calculations. However, at intermediate energies, i.e. energies of a few hundred MeV, and higher energies very many angular momenta contribute to the scattering amplitude. There those individual contributions to the scattering amplitude at a fixed high angular momentum oscillate strongly in angle, whereas the total amplitude is much smoother. This suggests the direct determination of  $T$  as function of the initial and final momentum vectors avoiding angular momentum decomposition totally. For NN scattering investigations of this kind have already been undertaken [1–4].

The choice of momentum vectors as adequate variables is also suggested from the NN force. The dependence on momentum vectors in the case of the widely used one-boson-exchange force is for instance rather simple, whereas the partial wave representation of this force leads to complicated expressions [5]. This is already apparent in the most simple case of a scalar meson propagator,  $1/((\mathbf{q}' - \mathbf{q})^2 - \mu^2)$ , which is the central ingredient to any NN force. In a partial wave decomposition this is represented in the form  $\frac{1}{q'q}Q_l(z)$ , where  $z = (\mathbf{q}'^2 + \mathbf{q}^2 + \mu^2)/2q'q$  and  $Q_l(z)$  is the Legendre function of the second kind. For large values of  $l$  the latter requires some care in order to be handled numerically correctly.

Scattering of more than two particles requires two-body t-matrices off-the-energy-shell (off-shell for short notation) as dynamical input, which are apparently easier to handle if they enter the calculations as smooth functions instead of strongly varying partial wave components. Of course those remarks also apply to the treatment of scattering processes of more than two particles at intermediate energies, which themselves are also treated more economically and transparently using momentum vectors instead of partial wave representations. Calculations of three and more particles use as input fully off-shell two-body t-matrices, whose properties as functions of arbitrary initial and final momenta and in general positive and negative energies should be well understood. Specifically at negative energies there may be bound state poles and in the second energy sheet there may be poles related to virtual states and resonances.

Our aim in this article is to generate two-body t-matrices directly in a three-dimensional form and display their properties as function of the magnitudes of the off-shell momenta, the angle between the two momentum vectors and of the energy. We are not aware of a similar study in this generality in the literature. Usually only partial wave projected amplitudes are displayed and discussed [6]. In Section II we describe our solution of the two-body Lippmann-Schwinger equation directly as function of the momentum vectors and illustrate the on- and off-shell properties of the resulting t-matrices obtained with simple Yukawa type two-nucleon potentials. In Section III we discuss the pole structure of the t-matrix as function of the energy and illustrate its angular and energy behavior at and around bound state poles. In Section IV we discuss and illustrate the behavior of the t-matrix for virtual and resonant states in the second energy sheet. We conclude in Section V.

## II. THE ON- AND OFF-SHELL TWO-BODY T-MATRIX AT POSITIVE ENERGIES

Two-body scattering is governed by the Lippmann-Schwinger equation

$$T = V + VG_0T, \quad (2.1)$$

where  $V$  is the two-body (e.g. two-nucleon) potential,  $G_0 = (z - H_0)^{-1}$  the free two-body propagator and  $T$  the transition operator. In momentum space its matrix elements  $T(\mathbf{q}', \mathbf{q}, z) \equiv \langle \mathbf{q}' | T(z) | \mathbf{q} \rangle$  obey the integral equation

$$T(\mathbf{q}', \mathbf{q}, z) = V(\mathbf{q}', \mathbf{q}) + \int d^3 q'' V(\mathbf{q}', \mathbf{q}'') \frac{1}{z - \frac{q''^2}{m}} T(\mathbf{q}'', \mathbf{q}, z). \quad (2.2)$$

Here  $\mathbf{q}$  are the relative momenta,  $m$  the common mass of the two particles and  $z$  an arbitrary energy. We use a nonrelativistic framework. In this article we restrict ourselves to two spinless particles and local potentials. Therefore,  $V(\mathbf{q}', \mathbf{q})$  as well as  $T(\mathbf{q}', \mathbf{q}, z)$  are scalar functions:

$$V(\mathbf{q}', \mathbf{q}) = V(q', q, \hat{\mathbf{q}}' \cdot \hat{\mathbf{q}}) \quad (2.3)$$

and

$$T(\mathbf{q}', \mathbf{q}) = T(q', q, \hat{\mathbf{q}}' \cdot \hat{\mathbf{q}}). \quad (2.4)$$

In Eq. (2.4) we dropped the parametric dependence on the energy  $z$ . This notation then leads to the explicit form of Eq. (2.2)

$$T(q', q, x') = V(q', q, x') + \int_0^\infty dq'' q''^2 \int_{-1}^1 dx'' \int_0^{2\pi} d\varphi'' V(q', q'', y) \frac{1}{z - \frac{q''^2}{m}} T(q'', q, x''), \quad (2.5)$$

where  $x' = \hat{\mathbf{q}}' \cdot \hat{\mathbf{q}}$ ,  $x'' = \hat{\mathbf{q}}'' \cdot \hat{\mathbf{q}}$ , and  $y = \hat{\mathbf{q}}'' \cdot \hat{\mathbf{q}}'$ . We can express  $y$  through  $x'$  and  $x''$  as

$$y = x' x'' + \sqrt{1 - x'^2} \sqrt{1 - x''^2} \cos \varphi'' \quad (2.6)$$

where the arbitrary azimuthal angle  $\varphi$  for  $\hat{\mathbf{q}}$  is chosen to be zero. If we define

$$v(q', q, x', x) \equiv \int_0^\infty d\varphi V(q', q, x' x + \sqrt{1 - x'^2} \sqrt{1 - x^2} \cos \varphi), \quad (2.7)$$

the integral equation Eq. (2.5) becomes

$$T(q', q, x') = \frac{1}{2\pi} v(q', q, x', 1) + \int_0^\infty dq'' q''^2 \int_{-1}^1 dx'' v(q', q'', x', x'') \frac{1}{z - \frac{q''^2}{m}} T(q'', q, x'') \quad (2.8)$$

This is a two-dimensional integral equation in the off-shell momenta  $q'$  ( $q''$ ) and the cosine of the ‘scattering angle’  $x'$  ( $x''$ ).

In this Section we consider the solutions of the integral equation Eq. (2.8) at positive energies, i.e. we choose  $z \equiv E + i\varepsilon = \frac{q_0^2}{m} + i\varepsilon$ , corresponding to the incoming momentum  $\mathbf{q}_0$ . In order to obtain insight into the behavior of the t-matrix, we will consider

the on-shell element  $T(q_0, q_0, x, E)$ , whose square is proportional to the differential cross section as well as the half-shell,  $T(q, q_0, x, E)$ , and fully off-shell,  $T(q, q', x, E)$  t-matrix.

We solve the two-dimensional integral equation typically using 24 or 32 q-points and 24 x-points. The Cauchy Singularity is separated into a principal value part and a  $\delta$ -function part, and the principal value singularity is treated by subtraction. The integration interval for the q-integration is covered by mapping the Gauss-Legendre points  $u$  from the interval (0,1) via  $q = c \tan(\frac{\pi}{2}u)$  to the interval (0,∞). Typical values of  $c$  are 1000 MeV/c.

A very stringent test for our numerics is the off-shell unitarity relation, which is a direct consequence of Eq. (2.2). In our two-dimensional form it reads

$$ImT(q', q, x') = -\frac{\pi}{2}mq_0 \int_{-1}^1 dx'' \int_0^{2\pi} d\varphi'' T(q', q_0, y) T^*(q, q_0, x'') \quad (2.9)$$

where  $y$  is given in Eq. (2.6). With Eq. (2.9) we allowed for the most general case of the unitarity relation, where the energy  $z = E = \frac{q_0^2}{m}$  is not related to the incoming momentum  $q$ , thus  $q \neq q' \neq q_0$ . In our numerical tests Eq. (2.9) was fulfilled for arbitrary  $q', q$ , and  $x'$  values with an accuracy below 0.001% with the above quoted number of integration points.

As main application we choose potentials of the Malfliet-Tjon [7] type, i.e.

$$V(r) = V_r \frac{e^{-\mu_R}}{r} - V_A \frac{e^{-\mu_A}}{r}, \quad (2.10)$$

and consequently

$$V(\mathbf{q}', \mathbf{q}) = \frac{1}{2\pi^2} \left( \frac{V_R}{(\mathbf{q}' - \mathbf{q})^2 + \mu_R^2} - \frac{V_A}{(\mathbf{q}' - \mathbf{q})^2 + \mu_A^2} \right). \quad (2.11)$$

In the case of a Malfliet-Tjon type potential the  $\varphi$ -integration of Eq. (2.7) can be carried out analytically with the result

$$v(q', q, x', x) = \frac{1}{\pi} \left[ \frac{V_R}{\sqrt{(q'^2 + q^2 - 2q'qx'x + \mu_R)^2 - 4q'^2q^2(1 - x'^2)(1 - x^2)}} \right. \quad (2.12) \\ \left. - \frac{V_A}{\sqrt{(q'^2 + q^2 - 2q'qx'x + \mu_A)^2 - 4q'^2q^2(1 - x'^2)(1 - x^2)}} \right].$$

The parameters used for  $V$  are given as  $V^{(I)}$  in Table I. Note that they are slightly different from the ones used in Ref. [7].

As first numerical example we would like to demonstrate the connection of the angle depended on-shell amplitude  $T(q_0, q_0, x, E)$  and its representation in terms of partial wave amplitudes,

$$T(q_0, q_0, x) = \sum_{l=0}^{\infty} \frac{2l+1}{4\pi} T_l(q_0) P_l(x), \quad (2.13)$$

where  $T_l(q_0) = \frac{2}{\pi} \frac{1}{q_0 m} e^{i\delta_l(q_0)} \sin \delta_l(q_0)$ . The quantity  $\delta_l(q_0)$  is the phase-shift for a given angular momentum  $l$  and is determined in a standard manner. In Fig. 1 we show  $Re T(q_0, q_0, x, E)$  at

300 and 800 MeV laboratory energies together with partial wave sums up to a given angular momentum  $l$ . Note that  $E = E_{lab}/2$ . The strong peak of  $Re T(q_0, q_0, x, E)$  in forward direction requires high orders of Legendre polynomials for a correct description. This is of course especially pronounced for the higher energy. In Fig. 2 we display  $Im T(q_0, q_0, x, E)$  at the same energies together with its representation in partial wave sums. It can be seen that  $Im T(q_0, q_0, x, E)$  needs less partial wave amplitudes for its correct representation, the reason being that  $Im T_l$  is proportional to  $\sin^2 \delta_l$ , whereas  $Re T_l$  is proportional to  $\cos \delta_l \sin \delta_l$ . For large values of  $l$  the phase shifts become small, thus  $Im T_l$  decreases with  $\delta_l^2$ , whereas  $Re T_l$  only decreases proportional to  $\delta_l$ .

An overview over the angular dependence of the full on-shell amplitude  $T(q_0, q_0, x, E)$  as function of the energy is given in Fig. 3. Starting from a relatively flat angular distribution at lower energies the peaking in forward direction develops with increasing energy. At the same time the angular range where the cross section is flat and small increases with increasing energy, indicating that forward scattering dominates at higher energies.

Next we consider the half-shell amplitude  $T(q, q_0, x, E)$  for two energies. Fig. 4 shows that  $T(q, q_0, x, E)$  is rather small and structureless for all off-shell momenta  $q$ , with the exception of  $q$  being close to the on-shell momentum  $q_0$ . The most general amplitude, the fully off-shell amplitude  $T(q, q', x, E)$  is displayed in Figs. 5 and 6 (the real part is shown) as function of one off-shell momentum  $q$  and the angle  $x$  for two fixed momenta  $q'$ . Contrary to what one might expect, the strongest forward peaking does not occur for  $q$  being close to on-shell, but for  $q = q'$ . This agrees with the behavior of the driving term, which peaks for  $q = q'$ . We found this behavior for all energies  $E > 0$ .

All numerical and graphical examples considered so far refer to a potential of Malfliet-Tjon type with repulsive and attractive parts (potential  $V^{(I)}$  in Table I). Its strength is such that it supports a bound state at  $E = -2.23$  MeV. Though this potential is of quite simple character, it captures essential features of NN interaction models based on meson exchange with respect to the propagator structure.

### III. THE OFF-SHELL T-MATRIX AT NEGATIVE ENERGIES

In the context of Faddeev-Yakubovsky equations two-body t-matrices need to be evaluated at negative energies. In a three-body system the energy argument for the two-body t-matrix is given as  $E = E_{tot} - \frac{3}{4m}q^2$  [9]. Here  $E_{tot}$  is the total energy of the three particle system and  $\frac{3}{4m}q^2$  is the kinetic energy of the relative motion of the third particle with respect to the interacting pair, which is described by the t-matrix. For an interacting three-body system the relative momentum  $|\mathbf{q}|$  is not conserved. Therefore it can have arbitrary values and  $E$  covers all energies below  $E_{tot}$ . Thus we are interested to see, whether the angular dependence of the t-matrix evaluated at negative energies is similar to the one observed at positive energies. A second consideration is that bound states of the two-body system lead to poles in the t-matrix. The angular dependence at and around a pole should be dictated by the one of the bound state. We will investigate these questions and provide numerical illustrations.

The formal solution to the Lippmann-Schwinger equation, Eq. (2.1), is given by

$$T(z) = V + V \frac{1}{z - H} V, \quad (3.1)$$

where  $H$  is the full two-body Hamiltonian. If this Hamiltonian supports a bound state  $|\phi_b\rangle$  at  $z = E_b$ , it follows immediately that

$$T(z) \xrightarrow{z \rightarrow E_b} V|\phi_b\rangle \frac{1}{z - E_b} \langle \phi_b|V. \quad (3.2)$$

In momentum space representation Eq. (3.2) reads

$$T(\mathbf{q}', \mathbf{q}, z) \xrightarrow{z \rightarrow E_b} \langle \mathbf{q}'|V|\phi_b\rangle \frac{1}{z - E_b} \langle \phi_b|V|\mathbf{q}\rangle. \quad (3.3)$$

The bound state obeys  $H|\phi_b\rangle = E_b|\phi_b\rangle$  and has a certain fixed angular momentum  $l$ , such that

$$\langle \mathbf{q}|\phi_b\rangle = \phi_{b,l}(q)Y_{lm}(\hat{\mathbf{q}}). \quad (3.4)$$

Since  $T$  is a scalar quantity, its behavior at and around the pole has to have the form

$$\begin{aligned} T(\mathbf{q}', \mathbf{q}, z) &\xrightarrow{z \rightarrow E_b} \sum_m Y_{lm}(\hat{\mathbf{q}}')g_l(q')\frac{1}{z - E_b}Y_{lm}^*(\hat{\mathbf{q}})g_l(q) \\ &= \frac{2l+1}{4\pi}P_l(\hat{\mathbf{q}}' \cdot \hat{\mathbf{q}})\frac{g_l(q')g_l(q)}{z - E_b} \\ &\equiv \frac{R_l(q', q, \hat{\mathbf{q}}' \cdot \hat{\mathbf{q}})}{z - E_b}. \end{aligned} \quad (3.5)$$

Here

$$g_l(q) = \int_0^\infty dq'q'^2v_l(q, q')\phi_{b,l}(q') \quad (3.6)$$

with

$$v_l(q, q') = \frac{2}{\pi} \int_0^\infty dr r^2 j_l(qr)V(r)j_l(q'r). \quad (3.7)$$

From Eq. (3.6) it can be clearly seen that the angular dependence of  $T$  exhibits a very characteristic behavior in the vicinity of the bound state poles, which is given by the Legendre function corresponding to the angular quantum number of the bound state. In order to illustrate the pole behavior, we choose the potential  $V^{(II)}$  of Table I, which supports a s-wave bound state at  $E_s = -190.16$  MeV and a p-wave bound state at  $E_p = -14.629$  MeV. These binding energies are determined in a standard manner solving the Schrödinger equation for a fixed angular momentum. This is a simple, one-dimensional problem, whose solution also provides the function  $g_l(q)$  and thus the residue  $R_l(q', q, \hat{\mathbf{q}}' \cdot \hat{\mathbf{q}})$  from Eq. (3.6). The values of the binding energies can also be obtained by solving the two-dimensional integral equation Eq. (2.8) and determining the pole position from the solution. Choosing the same integration points  $q$  in the partial wave projected, one-dimensional form and the two-dimensional form, the bound state energies  $E_b$  agree very well with the pole positions  $E_{pol}$ . For example, for 40 q-points (and 32 x-points) we find  $E_b(l=0) = -190.162$  MeV which has to be compared to  $E_{pol}(l=0) = -190.164$  MeV. Similarly, we find  $E_b(l=1) = -14.6296$  MeV compared to  $E_{pol}(l=1) = -14.6296$  MeV. These results can

be pushed to higher accuracy if desired. We also determine the residues at each pole from the solution of the two-dimensional integral equation and illustrate our result in Table II for the arbitrary choice of  $q' = q = q_0 = \sqrt{m|E|}$  and the angle averaged quantity  $\bar{T}_l \equiv \frac{1}{c_l} \int_{-1}^1 dx P_l(x) T(q_0, q_0, x, E) (E - E_{pol}(l))$ . As demonstrated in Table II, we approach the poles from both sides and the numbers closest to the poles agree very well with the corresponding residues calculated directly from the partial wave projected problem.

The angular dependence of  $T(q_0, q_0, x, E)$  with  $q_0 = \sqrt{m|E|}$  for energies close to the two poles is displayed in Fig. 7. Both figures show that near and at the pole the t-matrix shows the characteristic behavior of the Legendre function associated with the angular momentum quantum number of the corresponding bound state. In Fig. 8 we show the angular dependence of  $T(q_0, q_0, x, E)$  in the whole energy range around and in between the bound state poles. In order to include both poles we show  $(E - E_s)(E - E_p)T(q_0, q_0, x, E)$  in Figs. 7 and 8. Starting from very small values of  $|E|$ , the angular dependence is first of s-wave character, then turns to a p-wave shape at and near the p-wave pole and then develops the forward peak known from corresponding positive energies. Note that due to the multiplicative factors, the peak turns upward in the two figures. When  $|E|$  reaches the s-wave pole,  $T$  turns back to the pure s-wave behavior and then finally flips back into a strong forward peak.

The fact that the angular dependence at negative energies is reminiscent of that at the corresponding positive energies, except for the characteristic behavior near the poles, leads us to suspect that the real parts of  $T$  might be quite similar to each other at energies of equal magnitude. This turns out to be the case as demonstrated in Fig. 9, where we display  $\text{Re } T(q_0, q_0, x, E)$  for the potential  $V^{(I)}$  for different values  $|E|$ . It should be noted that the equality of  $\text{Re } T(q_0, q_0, x, E)$  for positive and negative energies is not the trivial consequence of  $\text{Re } T \approx V$ , which does not hold. In order to demonstrate that  $V$  is significantly different from  $\text{Re } T$ , we also display  $V$  in Fig. 9. Comparing  $\text{Re } T(q_0, q_0, x, E)$  at the different energies, we have to conclude that the rescattering terms,  $\text{Re } T - V$ , behave more and more similar to each other for the same absolute values of the energy.

Finally in Fig. 10 we display the real part of the fully off-shell t-matrix  $\text{Re } T(q, q', x, E)$  as function of  $q$  and  $x$  for fixed energy  $E = 200$  MeV and fixed momenta  $q' = 250$  MeV/c and  $q' = 1000$  MeV/c. As in Figs. 5 and 6 for positive energies  $\text{Re } T$  is most strongly peaked at  $q = q'$ , which can be expected once the information of Figs. 5 and 6 is known.

#### IV. THE OFF-SHELL T-MATRIX IN THE SECOND ENERGY SHEET

Two-body t-matrices might exhibit resonant behavior at positive energies or show a strong energy dependence near  $E = 0$  due to a virtual state. This latter case is realized for instance in the NN system for the partial wave state  ${}^1S_0$ . Our goal is to locate those resonances in the second energy sheet and investigate the characteristic angular dependence connected with the resonance or virtual state.

The transition to the second energy sheet requires an analytic continuation of the Lippmann-Schwinger equation, Eq. (2.2), into the second energy sheet, which we briefly describe here [9]. For a complex energy  $z$  located in the upper half plane, we modify the

integration path as indicated in Fig. 11. The contribution along the closed path II gives a residue and we find

$$\begin{aligned} T(\mathbf{q}', \mathbf{q}, z) &= V(\mathbf{q}', \mathbf{q}) - i\pi mq_z \int d\hat{q}'' V(\mathbf{q}', \hat{q}'' q_z) T(\hat{\mathbf{q}}'' q_z, \mathbf{q}, z) \\ &\quad + \int_{\cap} d^3 q'' V(\mathbf{q}', \mathbf{q}'') \frac{1}{z - \frac{q''^2}{m}} T(\mathbf{q}'', \mathbf{q}, z). \end{aligned} \quad (4.1)$$

Here  $q_z = \sqrt{mz}$ , and the symbol at the second integral indicates the deformed integration path I. Since we deformed the integration path such that it is located above the energy  $z$ , we are able to take  $z$  into the lower half of the complex plane without hitting a singularity in the propagator. Once the energy  $z$  is located in the lower half plane, we can return with the integration path I to the real axis and have instead of Eq. (4.1)

$$\begin{aligned} T(\mathbf{q}', \mathbf{q}, z) &= V(\mathbf{q}', \mathbf{q}) - i\pi mq_z \int d\hat{q}'' V(\mathbf{q}', \hat{\mathbf{q}}'' q_z) T(\hat{\mathbf{q}}'' q_z, \mathbf{q}, z) \\ &\quad + \int d^3 q'' V(\mathbf{q}', \mathbf{q}'') \frac{1}{z - \frac{q''^2}{m}} T(\mathbf{q}'', \mathbf{q}, z). \end{aligned} \quad (4.2)$$

This equation is valid on the second energy sheet, which is reached from the upper rim of the cut along the positive real energy axis in the physical sheet. Due to the additional imaginary term, Eq. (4.2) has to be supplemented by another equation, which we obtain by choosing  $\mathbf{q}' = \hat{\mathbf{q}} q_z$ ,

$$\begin{aligned} T(\hat{\mathbf{q}}' q_z, \mathbf{q}, z) &= V(\hat{\mathbf{q}}'' q_z, \mathbf{q}) - i\pi mq_z \int d\hat{q}'' V(\hat{\mathbf{q}}' q_z, \hat{\mathbf{q}}'' q_z) T(\hat{\mathbf{q}}'' q_z, \mathbf{q}, z) \\ &\quad + \int d^3 q'' V(\hat{\mathbf{q}}' q_z, \mathbf{q}'') \frac{1}{z - \frac{q''^2}{m}} T(\mathbf{q}'', \mathbf{q}, z). \end{aligned} \quad (4.3)$$

Similar to the bound state, which induces a nontrivial solution for the homogeneous equation related to Eq. (2.1), the homogeneous set of equations related to Eqs. (4.2) and (4.3) has a nontrivial solution at discrete values of  $z$ . These discrete values either correspond to resonances with  $\text{Re } z > 0$  and  $\text{Im } z < 0$  or to virtual states with  $\text{Re } z < 0$  and  $\text{Im } z = 0$ . The fact that this homogeneous set of equations has a nontrivial solution together with the compactness property of the integral kernel means that  $T(z)$  has a pole at those energies  $z$ . We are interested not only in determining the positions of those poles but also in understanding the residues and their angular dependence.

As it is obvious from Eq. (4.3), the driving term singles out the first entry as complex number. In order to simplify the formal steps leading to a determination of the residue, it is convenient to supplement the set of equations given in Eqs. (4.2) and (4.3) by another set in which the driving term has a complex entry in the second argument. The two sets can then be combined using the following matrix notation

$$\begin{aligned} \begin{pmatrix} T(\mathbf{q}', \mathbf{q}, z) & T(\mathbf{q}', \hat{\mathbf{q}}' q_z, z) \\ T(\hat{\mathbf{q}}' q_z, \mathbf{q}, z) & T(\hat{\mathbf{q}}' q_z, \hat{\mathbf{q}} q_z, z) \end{pmatrix} &= \begin{pmatrix} V(\mathbf{q}', \mathbf{q}) & V(\mathbf{q}', \hat{\mathbf{q}}' q_z) \\ V(\hat{\mathbf{q}}' q_z, \mathbf{q}) & V(\hat{\mathbf{q}}' q_z, \hat{\mathbf{q}} q_z) \end{pmatrix} \\ &\quad + \begin{pmatrix} \int d^3 q'' V(\mathbf{q}', \mathbf{q}'') & q_z^3 \int d\hat{q}'' V(\mathbf{q}', \hat{\mathbf{q}}'' q_z) \\ \int d^3 q'' V(\hat{\mathbf{q}}' q_z, \mathbf{q}'') & q_z^3 \int d\hat{q}'' V(\hat{\mathbf{q}}' q_z, \hat{\mathbf{q}}'' q_z) \end{pmatrix} \\ &\quad \times \begin{pmatrix} \frac{1}{z - \frac{q''^2}{m}} & 0 \\ 0 & -i\pi \frac{m}{q_z^2} \end{pmatrix} \begin{pmatrix} T(\mathbf{q}'', \mathbf{q}, z) & T(\mathbf{q}'', \hat{\mathbf{q}} q_z, z) \\ T(\hat{\mathbf{q}}'' q_z, \mathbf{q}, z) & T(\hat{\mathbf{q}}'' q_z, \hat{\mathbf{q}} q_z, z) \end{pmatrix}. \end{aligned} \quad (4.4)$$

Introducing the appropriate matrices, we write Eq. (4.4) as

$$\tilde{\mathbf{T}} = \tilde{\mathbf{V}} + \tilde{\mathbf{V}}\tilde{\mathbf{G}}\tilde{\mathbf{T}}. \quad (4.5)$$

We also need to study the corresponding homogeneous problem, which we want to write in the following form

$$\lambda(z)\tilde{\chi} = \tilde{\mathbf{V}}\tilde{\mathbf{G}}\tilde{\chi}. \quad (4.6)$$

In this form the eigenvalue is  $\lambda(z)$  and the energy  $z$  is a parameter. Since  $\tilde{\mathbf{V}}\tilde{\mathbf{G}}$  is a compact operator, there is a discrete set of eigenvalues, which accumulate at  $\lambda(z) = 0$  [10]. The physical resonances occur at those values  $z \equiv E_{res}$ , for which  $\lambda(E_{res}) = 1$ .

In the following we choose  $z = E_{res}$ . Then we have

$$\tilde{\chi} = \tilde{\mathbf{V}}\tilde{\mathbf{G}}\tilde{\chi}. \quad (4.7)$$

Since the kernel is nonsymmetric, we also have to consider the left hand eigenvalue problem

$$\tilde{\Theta}^T = \tilde{\Theta}^T \tilde{\mathbf{V}} \tilde{\mathbf{G}}. \quad (4.8)$$

Defining

$$\tilde{\Phi}^T \equiv \tilde{\Theta}^T \tilde{\mathbf{V}} \quad (4.9)$$

we deduce

$$\tilde{\Phi}^T = \tilde{\Phi}^T \tilde{\mathbf{G}} \tilde{\mathbf{V}} \quad (4.10)$$

or

$$\tilde{\Phi} = \tilde{\mathbf{V}}^T \tilde{\mathbf{G}} \tilde{\Phi}. \quad (4.11)$$

Since  $\tilde{\mathbf{V}}^T = \tilde{\mathbf{V}}$ , we obtain  $\tilde{\Phi} = \tilde{\chi}$ .

In the immediate neighborhood of  $z = E_{res}$  and as a consequence of

$$\tilde{\mathbf{T}}(z) = (1 - \tilde{\mathbf{V}}\tilde{\mathbf{G}})^{-1}\tilde{\mathbf{V}} \quad (4.12)$$

one has

$$\tilde{\mathbf{T}}(z) \xrightarrow{z \rightarrow E_{res}} \tilde{\chi}(1 - \lambda(z))^{-1} \frac{1}{N} \tilde{\Theta}^T \tilde{\mathbf{V}}, \quad (4.13)$$

where  $N$  is a normalization factor. In the neighborhood of  $z = E_{res}$  we can put

$$\lambda(z) \approx 1 + \lambda'(z) \Big|_{z=E_{res}} (z - E_{res}) \quad (4.14)$$

and obtain

$$\tilde{\mathbf{T}}(z) \xrightarrow{z \rightarrow E_{res}} \tilde{\chi} \frac{1}{z - E_{res}} \frac{-1}{\lambda'(z) \Big|_{z=E_{res}}} \frac{1}{N} \tilde{\chi}^T. \quad (4.15)$$

For the case of a bound state pole it is easy to prove that  $\frac{-1}{\lambda'(z)|_{z=E_{res}}}\frac{1}{N} = 1$  for a normalized bound state  $|\phi_b\rangle$  and  $|\chi\rangle = V|\phi_b\rangle$ . If we consider the right hand side of Eq. (4.15) as function of an auxiliary strength factor to the potential, we can adopt the normalization of the bound state and define

$$\tilde{\mathbf{T}}(z) \xrightarrow{z \rightarrow E_{res}} \tilde{\chi} \frac{1}{z - E_{res}} \tilde{\chi}^T. \quad (4.16)$$

The final remark concerns the scalar nature of  $\tilde{\mathbf{T}}(\mathbf{q}', \mathbf{q}, z)$ . Since a resonant state has a unique angular momentum  $l$ , the function  $\chi(\mathbf{q})$  will have the form

$$\chi(\mathbf{q}) = \chi_l(q) Y_{lm}(\hat{\mathbf{q}}), \quad (4.17)$$

and we have to conclude that

$$\tilde{\mathbf{T}}(\mathbf{q}', \mathbf{q}, z) \xrightarrow{z \rightarrow E_{res}} \frac{2l+1}{4\pi} \chi_l(q') \frac{1}{z - E_{res}} \chi_l(q) P_l(\hat{\mathbf{q}}' \cdot \hat{\mathbf{q}}). \quad (4.18)$$

If  $ReE_p > 0$  and if  $ImE_p < 0$  sufficiently small, the the t-matrix will feel the nearby pole also for real, positive energies  $z$ , and a resonance will occur in the differential cross section. In the case of a virtual state, like for  ${}^1S_0$  in NN scattering, the pole is located at  $ReE_p < 0$  and  $ImE_p = 0$ . For sufficiently small values of  $|ReE_p|$  the t-matrix will be strongly enhanced near and at  $z = 0$ .

For our numerical realization we rewrite Eqs. (4.2) and (4.3) analogously to Eq. (2.8) as

$$\begin{aligned} T(q', q, x') &= \frac{1}{2\pi} v(q', q, x, 1) \\ &+ \int_0^\infty dq'' q''^2 \int_{-1}^1 dx'' v(q', q'', x', x'') \frac{1}{z - \frac{q''^2}{m}} T(q'', q, x'') \\ &- i\pi m q_z \int_{-1}^1 dx'' v(q', q_z, x', x'') T(q_z, q, x'') \end{aligned} \quad (4.19)$$

and

$$\begin{aligned} T(q_z, q, x') &= \frac{1}{2\pi} v(q_z, q, x, 1) \\ &+ \int_0^\infty dq'' q''^2 \int_{-1}^1 dx'' v(q_z, q'', x', x'') \frac{1}{z - \frac{q''^2}{m}} T(q'', q, x'') \\ &- i\pi m q_z \int_{-1}^1 dx'' v(q_z, q_z, x', x'') T(q_z, q, x''). \end{aligned} \quad (4.20)$$

Here  $z \equiv E = |E|e^{i\phi}$  with  $\phi < 0$  and  $q_z = \sqrt{mE} = \sqrt{m|E|}e^{i\phi/2}$ . The nontrivial solution to the homogeneous system of Eq. (4.7) has a fixed angular momentum. When employing Eq. (4.17), we obtain

$$\chi_l(q) = \int_0^\infty dq' q'^2 v_l(q, q') \frac{1}{z - \frac{q'^2}{m}} \chi_l(q') - i\pi m q_z v_l(q, q_z) \chi_l(q_z) \quad (4.21)$$

and

$$\chi_l(q_z) = \int_0^\infty dq' q'^2 v_l(q_z, q') \frac{1}{z - \frac{q'^2}{m}} \chi_l(q') - i\pi m q_z v_l(q_z, q_z) \chi_l(q_z). \quad (4.22)$$

We used the above given equations Eqs. (4.21) and (4.22) to determine the location of the resonances in the second energy sheet. For s-waves they are usually called virtual states and are located on the negative energy axis. For partial waves with  $l = 1$  or higher, the energy eigenvalues have a positive real part and a negative imaginary part. For varying potential strength, they move along trajectories in the complex energy plane. In the following, we numerically study two different cases, namely a s-wave virtual state supported by potential model  $V^{(V)}$  of Table I and a p-wave resonance of potential model  $V^{(IV)}$  of Table I. The corresponding trajectories are listed in Table III and shown in Fig. 12.

For the case of the s-wave virtual state we started from potential model  $V^{(V)}$  of Table I. The s-wave phase shift of this potential has an effective range expansion with a scattering length  $a_s = -23.5818$  fm and an effective range  $r_s = 2.8789$  fm. Using these values, the pole position for the S-matrix can be estimated via the effective range expansion as

$$q_v^a = i \left[ \frac{1}{r_s} - \sqrt{\frac{2}{r_s |a_s|} + \frac{1}{r_s^2}} \right], \quad (4.23)$$

which leads in our specific case to a position of the virtual state  $E_{qv}^a = -\frac{(q_v^a)^2}{m} = -0.06738$  MeV, where we used  $m = 938.9$  MeV. This number is very close to the exactly calculated value given as  $E_p(l = 0) = -0.06663$  MeV, which is given in Table III. In the same table we quantify the s-wave trajectory as a function of the strength parameter  $V_A$  of potential  $V^{(V)}$ .

For obtaining a p-wave resonance state, we start from potential  $V^{(III)}$  of Table I, which supports a p-wave bound state, and decrease the attraction by decreasing the strength parameter  $V_A$  until the bound state turns into a resonance state. Selected values for the so obtained trajectory for the p-wave resonance are listed in Table III. Of course, this model does not correspond to the reality of an NN force, even for the lowest value of  $V_A = 4.7$  given in Table III, the binding energy of the s-wave bound state is still  $E_s = -52.52$  MeV. Nevertheless, this example illustrates in a simple manner, what can be expected for other cases like an effective nucleon-nucleus interaction, which supports low energy resonances for certain angular momentum states. Qualitatively the same picture would emerge.

We would like to mention that we solved the homogeneous set of Eqs. (4.21) and (4.22) by the very efficient power method [7,9]. Regarding the notation of Eq. (4.7), one has to determine the eigenvalue  $\lambda(z)$  and vary the energy such that  $\lambda(z) = 1$ . For the potentials used here, the largest eigenvalue in magnitude was always an unphysical one with a negative real part generated by the repulsive short range piece of the force. Once the largest eigenvalue is determined, we introduce a new integral kernel, consisting of the old one minus that specific eigenvalue. The in this way defined new kernel has then the physical eigenvalue as the largest one in magnitude.

Next we investigate the solution of the t-matrix in the second energy sheet as given by Eqs. (4.19) and (4.20). We are interested in verifying the location of the pole as well as the angular dependence of the residue at the pole as given in Eq. (4.18). We

illustrate our findings for the potential  $V^{(IV)}$  of Table I, which has a p-wave resonant state at  $E_{res}(l=1) = (4.3177 - i2.2386)$  MeV and for the potential  $V^{(V)}$  of Table I, which has a virtual s-wave state at  $E_{res}(l=0) = -0.06663$  MeV. For the p-wave resonance we show in Figs. 13 and 14 the angular dependence of  $Re [(E - E_{res}(l=1))T(q_E, q_0, x, E)]$  as function of the complex energy  $E$  located along two straight lines going through the pole position. In Fig. 13 we start on the real axis at  $E = 4.3$  MeV and successively increase the imaginary part of  $E$ . For  $E = (4.3 - i2.4)$  MeV we clearly see an angular dependence characteristic of a p-wave residue. Since the width of the resonance is relatively small, the p-wave behavior is present along the whole vertical energy line including the point on the real axis. For our second choice of energy line (Fig. 14), a declined line starting from zero energy, starts with a behavior being a mixture of s- and p-wave, but still relatively flat. Approaching the resonance, the shape becomes predominantly the one of a  $P_1(x)$  given by the p-wave residue.

A corresponding study based on the potential model  $V^{(V)}$  is shown in Fig. 15 for the negative real axis in the second sheet, where the neighborhood of the virtual pole position is considered. In the vicinity of the virtual state, the residue exhibits perfect s-wave characteristics.

Finally, we would like to demonstrate the structure of the t-matrix as given in Eq. (4.18) in a numerical example. First, we numerically verify that  $\lim_{z \rightarrow E_{res}} (z - E_{res})T(q', q, x, z)$  behaves like  $P_1(z)$ . Then we determine  $\chi_1(q)$  by comparing the numerically calculated quantity  $(z - E_{res})T(q', q, x, z)$  to the form given in Eq. (4.18). Instead of dividing by  $P_1(x)$  we use

$$\bar{\chi}_1(q) = \lim_{z \rightarrow E_{res}} \sqrt{2\pi \int_{-1}^1 dx P_1(x)(z - E_{res})T(q, q, x, z)}. \quad (4.24)$$

The values of  $\bar{\chi}_1(q)$  for  $z$  approaching  $E_{res}$  are shown for a few arbitrarily selected momentum points  $q$  in Table IV. They stabilize for  $z$  approaching the pole position  $E_{res} = (4.318 - i2.239)$  MeV. The last row in Table IV shows the values obtained from the solution of the homogeneous set of Eqs. (4.21) and (4.22). They have been normalized at one  $q$  point to the  $\chi_1(q)$  extracted from  $T(q, q, x, z \rightarrow E_{res})$ . The agreement is perfect.

Finally, we directly verified the separable structure of  $T(q', q, x, z \rightarrow E_{res})$  as given in Eq. (4.18) by evaluating  $\tilde{T} = 2\pi \int_{-1}^1 dx P_1(x)(E - E_{res})T(q', q, x, E)$  very close to  $E = E_{res}$  for different  $q' \neq q$  and comparing them to the values obtained via Table IV. The agreement is again perfect and the values for a selected set of momentum points  $q'$  and  $q$  are given in Table V.

## V. SUMMARY

Two nucleon scattering at intermediate energies of a few hundred MeV requires quite a few angular momentum states in order to achieve convergence of e.g. scattering observables. This is even more true for the scattering of three or more nucleons upon each other. An alternative approach to the conventional one, which is based on angular momentum decomposition, is to work directly with momentum vectors, specifically with the magnitudes of the momenta and the angles between them. We formulated and numerically illustrated this alternative approach for the case of two-body scattering, which includes the

approach towards bound states and resonances. The angular dependence of the two-body t-matrix is directly determined from the Lippmann-Schwinger equation, which now is a two-dimensional integral equation in contrast to the one-dimensional one for a fixed angular momentum in a partial wave formulation. This two-dimensional integral equation is quite easily numerically tractable. We determined the angular dependence of the on-shell, half-shell and fully off-shell t-matrix as function of the scattering energy and different choices of momenta. As two-body force we concentrated on a superposition of an attractive and repulsive Yukawa interaction, which is typical for nuclear physics. We neglected spin degrees of freedom in all our studies.

We want to briefly summarize our results. The on-shell t-matrix develops a strong forward peak as the energy increases, which is more and more difficult to build up in a calculation based on angular momentum decomposition, but relatively simple accessible in our approach using momentum vectors. The angular dependence of a half-shell t-matrix is strong only around the on-shell momentum and rather mild otherwise. For a fully off-shell t-matrix  $T(q, q', x, E)$  the strong angular dependence occurs for  $q = q'$ , which do not necessarily have to coincide with the on-shell momentum. At negative energies the t-matrix has poles located at the bound state energies, if those exist. As example we investigated s- and p-wave bound states. The numerically determined t-matrix turned out to be very well under control even quite close to the the bound state poles, where the homogeneous version of the Lippmann-Schwinger equation has a nontrivial solution. We determined the angular dependence of the t-matrix at the two poles, at energies between them and at energies way below the deepest bound state. Directly at the poles the angular behavior displays the characteristics of the Legendre polynomial of the same angular momentum  $l$  as the bound state. Between the poles as well as for energies below the last bound state the t-matrix exhibits the same forward peaking as visible at positive energies. This latter result is interesting by itself. The angular dependence at positive and negative energies is very similar. More quantitatively, we found that the real parts of the t-matrix are extremely close to each other at positive and negative energies of equal magnitude long before this statement becomes trivial due to the validity of the Born approximation  $T = V$ .

Finally we studied the analytical continuation of the Lippmann-Schwinger equation into the second energy sheet, which is reached through the cut along the positive real axis of the physical sheet. In the lower half plane possible resonance poles of the t-matrix are located, which are of course of interest only if they are close to the real axis. As example we studied a p-wave resonance and mapped out its pole trajectory by varying the potential strength. At the pole, the t-matrix achieves a separable form, which we verified numerically. We also verified the characteristic angular dependence of the t-matrix close to the resonance, which corresponds to the Legendre polynomial of degree  $l$  of the angular momentum state of the resonance. For negative energies in the second sheet we investigated the pole trajectory of a virtual s-wave state, which is of interest in the NN system for the quantum number  $^1S_0$ .

Summarizing we can state that the two-dimensional Lippmann-Schwinger equation can be handled quite easily in a numerically very reliable manner. In this approach one determines directly the angular dependence of the t-matrix for arbitrary momenta and energies. Once supplemented by spin degrees of freedom this approach will be of interest in the NN system. In addition, this approach will be generalizable to systems with three particles, like three nucleons or two nucleons and a meson. In the case of three nucleons,

Faddeev calculations at e.g. 150 MeV and higher are getting quite tedious because of the very many orbital angular momentum states involved [8] and a direct, three-dimensional approach appears to be preferable. First steps in this direction are under way.

#### **ACKNOWLEDGMENTS**

This work was performed in part under the auspices of the U. S. Department of Energy under contract No. DE-FG02-93ER40756 with Ohio University and the NATO Collaborative Research Grant 960892. We thank the Ohio Supercomputer Center (OSC) for the use of their facilities under Grant No. PHS206. The authors would like to thank S.P. Weppner and X.D. Zhang for their help in preparing some of the figures.

## REFERENCES

- [1] J. Holz and W. Glöckle, Phys. Rev **C37**, 6 (1988); J. Holz and W. Glöckle, J. Comp. Phys. **76**, 131 (1988).
- [2] R.A. Rice and Y.E. Kim, Few-Body Syst. **14**, 127 (1993).
- [3] J. Hiltrop, Diploma Thesis, Bochum, 1989, unpublished; I. Posukidis, Diploma Thesis, Bochum, 1993, unpublished.
- [4] D. Hüber, W. Glöckle, and A. Bömelburg, Phys. Rev **C42**, 2342 (1990).
- [5] R. Machleidt, K. Holinde, Ch. Elster, Phys. Rep. **149**, 1 (1987).
- [6] E.F. Redish and K. Stricker-Bauer, Phys. Rev. **C36**, 513 (1987).
- [7] R.A. Malfliet and J.A. Tjon, Nucl. Phys. **A127**, 161 (1969).
- [8] W. Glöckle, H. Witala, D. Hüber, H. Kamada, J. Golak, Phys. Rep. **274**, 107 (1996).
- [9] W. Glöckle, The Quantum Mechanical Few-Body Problem, Springer Verlag, 1983.
- [10] S. Weinberg, Phys. Rev **133B**, 232 (1964).

## TABLES

TABLE I. Parameters of the Malfliet-Tjon type potentials. As conversion factor we use units such that  $\hbar c=197.3286$  MeVfm=1.

	$V_A$	$\mu_A$ [MeV]	$V_R$	$\mu_R$ [MeV]
$V^{(I)}$	3.1769	305.86	7.291	613.69
$V^{(II)}$	-	-	10.0	2000.
$V^{(III)}$	6.0	305.86	7.291	613.69
$V^{(IV)}$	5.1	305.86	7.291	613.69
$V^{(V)}$	2.6047	305.86	7.291	613.69

TABLE II. Determination of  $\bar{T}_l \equiv 1/c_l \int_{-1}^1 dx P_l(x) T(q_0, q_0, x, E) (E - E_{pol}(l))$  as function of  $E$  close to the  $l = 1$  and  $l = 0$  poles. The values for the constants are  $c_0=2$  and  $c_1=2/3$ . The entry p.w. indicates the value determined from the partial wave projected problem.

$E$ [MeV]	$\hat{T}_1(E)$ [MeV fm $^2$ ]	$E$ [MeV]	$\hat{T}_0(E)$ [MeV fm $^2$ ]
-14.60	1.08424	-189.8	4.37911
-14.61	1.08513	-189.9	4.37847
-14.62	1.08597	-190.0	4.37772
-14.63	1.08588	-190.1	4.37722
-14.64	1.08778	-190.2	4.37693
-14.65	1.08857	-190.3	4.37608
p.w.	1.08684	p.w.	4.37685

TABLE III. Pole trajectories in the complex energy plane as function of the strength parameter  $V_A$  for the potentials  $V^{(III)}$  (p-wave pole trajectory) and  $V^{(V)}$  (s-wave virtual state trajectory).

$V_A$ ( $V^{(III)}$ )	$E_{res}(l=1)$ [MeV]	$V_A$ ( $V^{(V)}$ )	$E_{res}(l=0)$ [MeV]
5.4	0.9267 -i 0.1821	2.6047	-0.06663
5.3	2.1972 -i 0.7101	2.6	-0.07380
5.2	3.3254 -i 1.4134	2.5	-0.31004
5.1	4.3177 -i 2.2386	2.4	-0.69870
5.0	5.1801 -i 3.1552	2.3	-1.22970
4.9	5.9178 -i 4.1413	2.2	-1.89209
4.8	6.5358 -i 5.1806	2.1	-2.67878
4.7	7.0388 -i 6.2597	2.0	-3.57733

TABLE IV. Determination of  $\bar{\chi}_1(q)$  in the vicinity of the p-wave resonance of potential model  $V^{(IV)}$  as function of the complex energy E.

E [MeV]	$\bar{\chi}_1(q=94.89 \text{ MeV}/c)$	$\bar{\chi}_1(q=292.73 \text{ MeV}/c)$	$\bar{\chi}_1(q=527.50 \text{ MeV}/c)$	$\bar{\chi}_1(q=758.09 \text{ MeV}/c)$
4.32 -i 2.0	1.105 -i 0.400	1.856 -i 0.729	1.149 -i 0.473	0.491 -i 0.212
4.32 -i 2.10	1.103 -i 0.400	1.851 -i 0.729	1.144 -i 0.471	0.488 -i 0.207
4.32 -i 2.20	1.101 -i 0.400	1.846 -i 0.729	1.139 -i 0.468	0.484 -i 0.202
4.32 -i 2.23	1.101 -i 0.400	1.844 -i 0.729	1.138 -i 0.467	0.483 -i 0.201
4.32 -i 2.4	1.098 -i 0.400	1.835 -i 0.729	1.129 -i 0.461	0.477 -i 0.192
4.32 -i 2.5	1.096 -i 0.400	1.830 -i 0.729	1.124 -i 0.459	0.473 -i 0.187
p.w.	1.102 -i 0.400	1.844 -i 0.729	1.138 -i 0.468	0.482 -i 0.200

TABLE V. Comparison of  $\bar{T} = 2\pi \int_{-1}^1 dx P_1(x)(E - E_{res})T(q, q', x, E)$  with  $\bar{\chi}_1(q)\bar{\chi}_1(q')$  for a fixed value  $q'$  and different values of  $q$  at the p-wave resonance of potential model  $V^{(IV)}$ . The energy E for calculating  $\bar{T}$  was fixed at  $E = (4.32 - i2.23) \text{ MeV}$ .

q [MeV/c]	q' [MeV/c]	$\bar{T}[\text{MeV fm}^2]$	$\bar{\chi}_1(q)\bar{\chi}_1(q')[\text{MeV fm}^2]$
292.73	94.89	1.7398 -i 1.5395	1.7397 -i 1.5398
527.50	94.89	1.0668 -i 0.9683	1.0667 -i 0.9689
758.09	94.89	0.4522 -i 0.4134	0.4521 -i 0.4140

## FIGURES

FIG. 1. Angular dependence for the real part of the on-shell t-matrix,  $Re T(q_0, q_0, x, E)$ . At  $E_{lab} = 300$  MeV (a) the dashed line represents the partial wave sum up to  $j = 2$ , the dash-dotted line the sum up to  $j = 4$  and the solid line the sum up to  $j = 6$ . The solid bullets stand for the 3D calculation. At  $E_{lab} = 800$  MeV (b) the dashed line represents the partial wave sum up to  $j = 6$ , the dash-dotted line stands for the sum up to  $j = 9$ , and the solid line for the sum up to  $j = 12$ . Again, the solid bullets represent the 3D calculation.

FIG. 2. Angular dependence for the imaginary part of the on-shell t-matrix,  $ImT(q_0, q_0, x, E)$ . At  $E_{lab} = 300$  MeV (a) the dashed line represents the partial wave sum up to  $j = 2$ , the solid line the sum up to  $j = 4$ . The solid bullets stand for the 3D calculation. At  $E_{lab} = 800$  MeV (b) the dashed line represents the partial wave sum up to  $j = 3$ , the solid line the sum up to  $j = 6$ . The bullets stand for the 3D calculation.

FIG. 3. The angular dependence of the on-shell t-matrix as function of the laboratory energy from  $E_{lab} = 50$  MeV to  $E_{lab} = 1000$  MeV. On the left  $ReT(q_0, q_0, x, E_{lab})$  is displayed, on the right  $ImT(q_0, q_0, x, E_{lab})$ .

FIG. 4. The angular dependence for the real part of the half-shell t-matrices,  $Re T(q, q_0, x, E)$ , is displayed for  $E_{lab} = 200$  MeV (a) and  $E_{lab} = 500$  MeV (b).

FIG. 5. The angular dependence for the real part of the off-shell t-matrix,  $Re T(q, q' = 250 MeV/c, x, E)$ , is displayed for  $E_{lab} = 400$  MeV.

FIG. 6. The angular dependence for the real part of the off-shell t-matrix,  $Re T(q, q' = 1000 MeV/c, x, E)$ , is displayed for  $E_{lab} = 400$  MeV.

FIG. 7. The angular dependence for  $(E - E_s)(E - E_p)T(q_0, q_0, x, E)$  for energies  $E$  around the p-wave pole (a) and the s-wave pole (b).

FIG. 8. The angular dependence for  $(E - E_s)(E - E_p)T(q_0, q_0, x, E)$  as function of the energy from  $E = -200$  MeV to  $E = -1$  MeV. Note the characteristic angular behavior around the p- and s-wave poles as well as the strong forward peak between the two poles and below the s-wave pole.

FIG. 9. The angular dependence for the real part of the on-shell t-matrix  $Re T(q_0, q_0, x, E)$  for  $|E| = 200, 400$  and  $800$  MeV. For comparison, the angular dependence of the driving term,  $V^I$ , is also shown as dash-dotted line.

FIG. 10. The angular dependence for the real part of the off-shell t-matrix  $Re T(q, q', x, E = 200 MeV)$  is displayed for  $q' = 250$  MeV/c (a) and for  $q' = 1000$  MeV/c (b).

FIG. 11. Modified integration path in the complex  $q$  plane for the analytic continuation of the Lippmann-Schwinger equation into the second energy sheet as described in the text.

FIG. 12. The pole trajectories of the p-wave and s-wave pole in the second energy sheet as given by the potentials  $V^{(IV)}$  and  $V^{(V)}$  of Table I.

FIG. 13. The angular dependence for the real part of  $(E - E_{res})T(q_E, q_0, x, E)$  as function of the complex energy  $E$  around the p-wave resonance of potential model  $V^{(IV)}$ . The off-shell momentum  $q_0$  is fixed at 100 MeV/c.

FIG. 14. Same as Fig. 13, but for a different path of the complex energy  $E$ .

FIG. 15. The angular dependence of  $(E - E_{res})T(q_E, q_0, x, E)$  as function of the negative energy  $E$  in the second energy sheet around the s-wave virtual state of potential model  $V^{(V)}$ . The off-shell momentum  $q_0$  is fixed at 100 MeV/c.

Fig. 1a

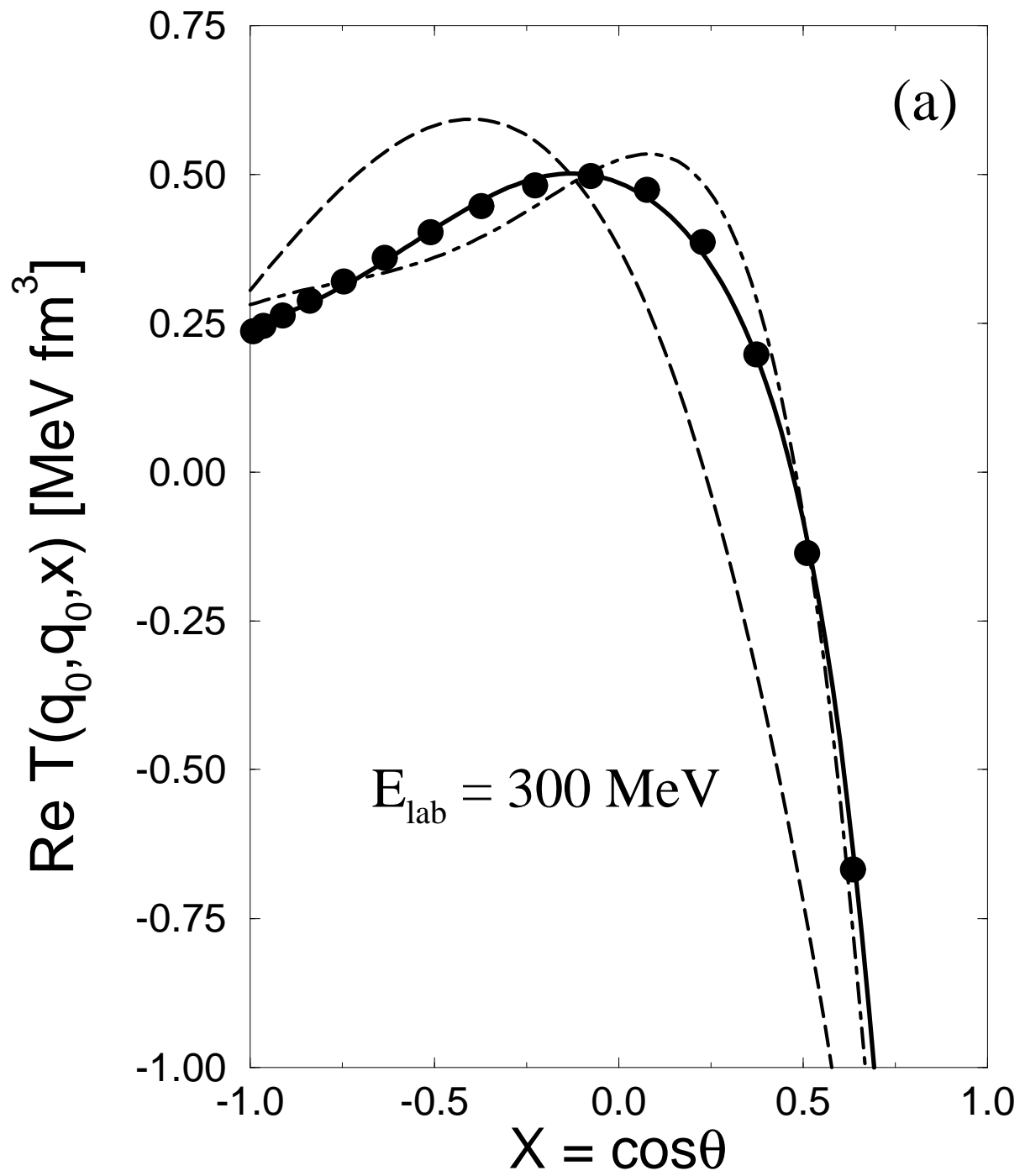


Fig. 1b

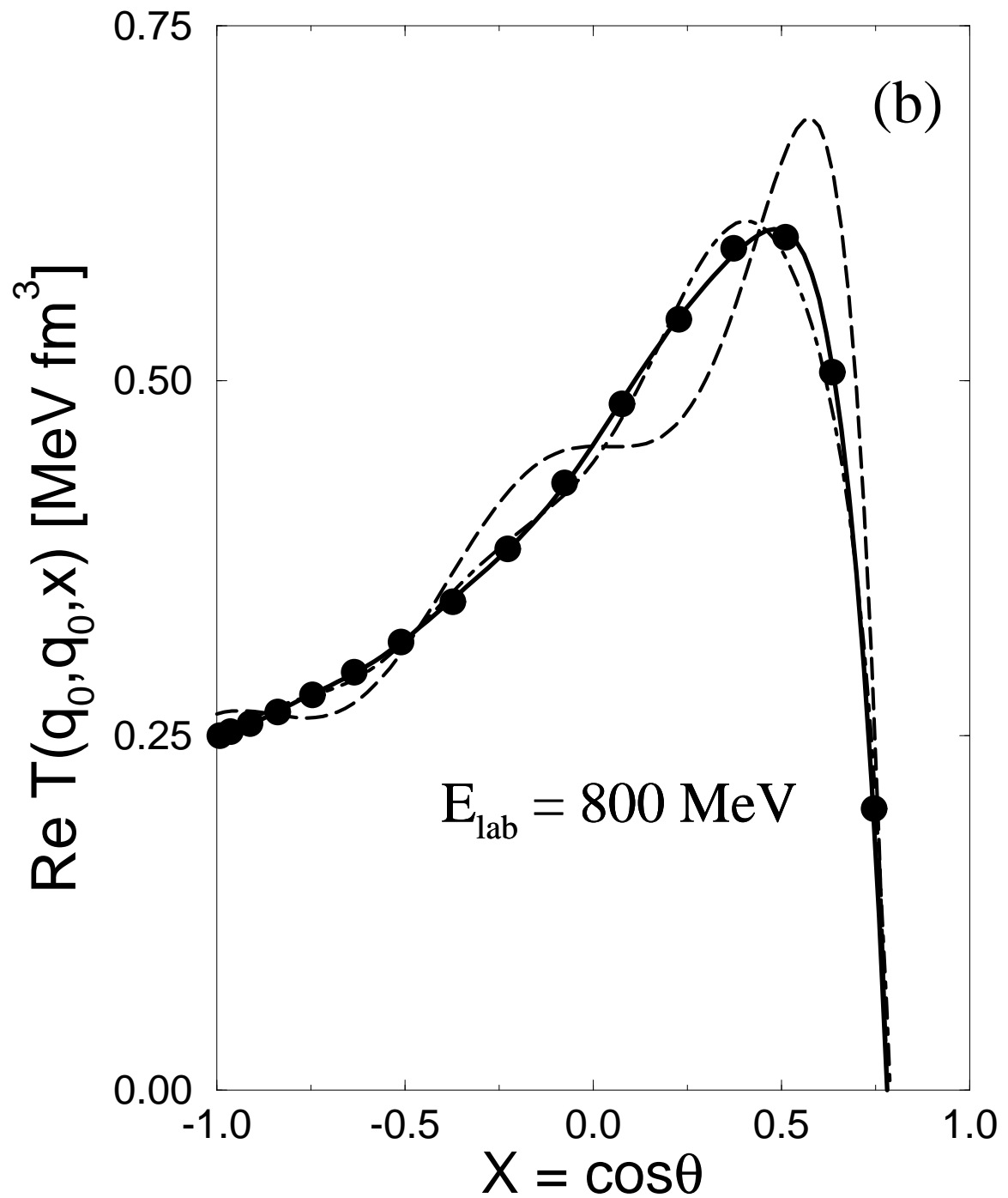


Fig. 2a

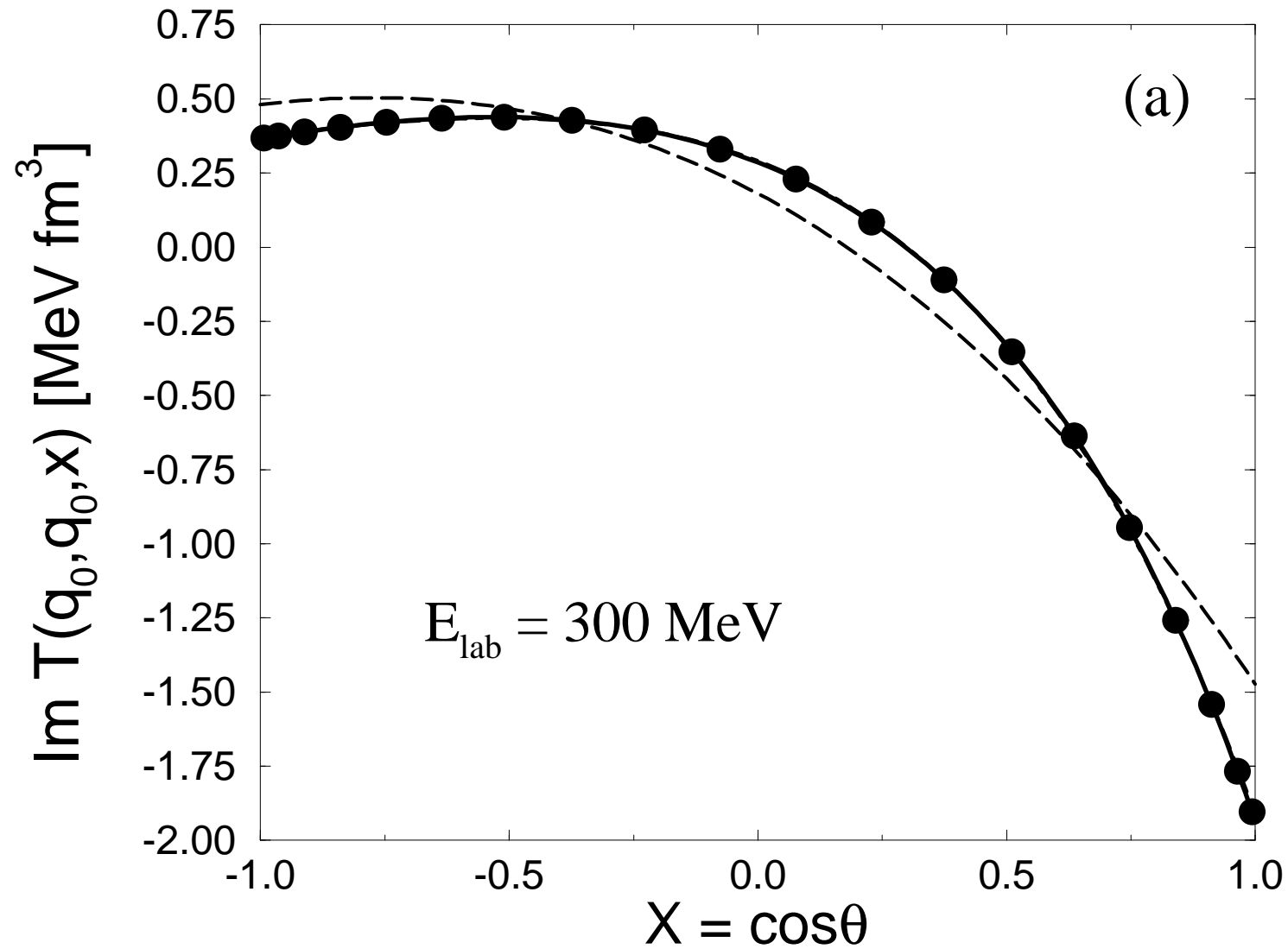
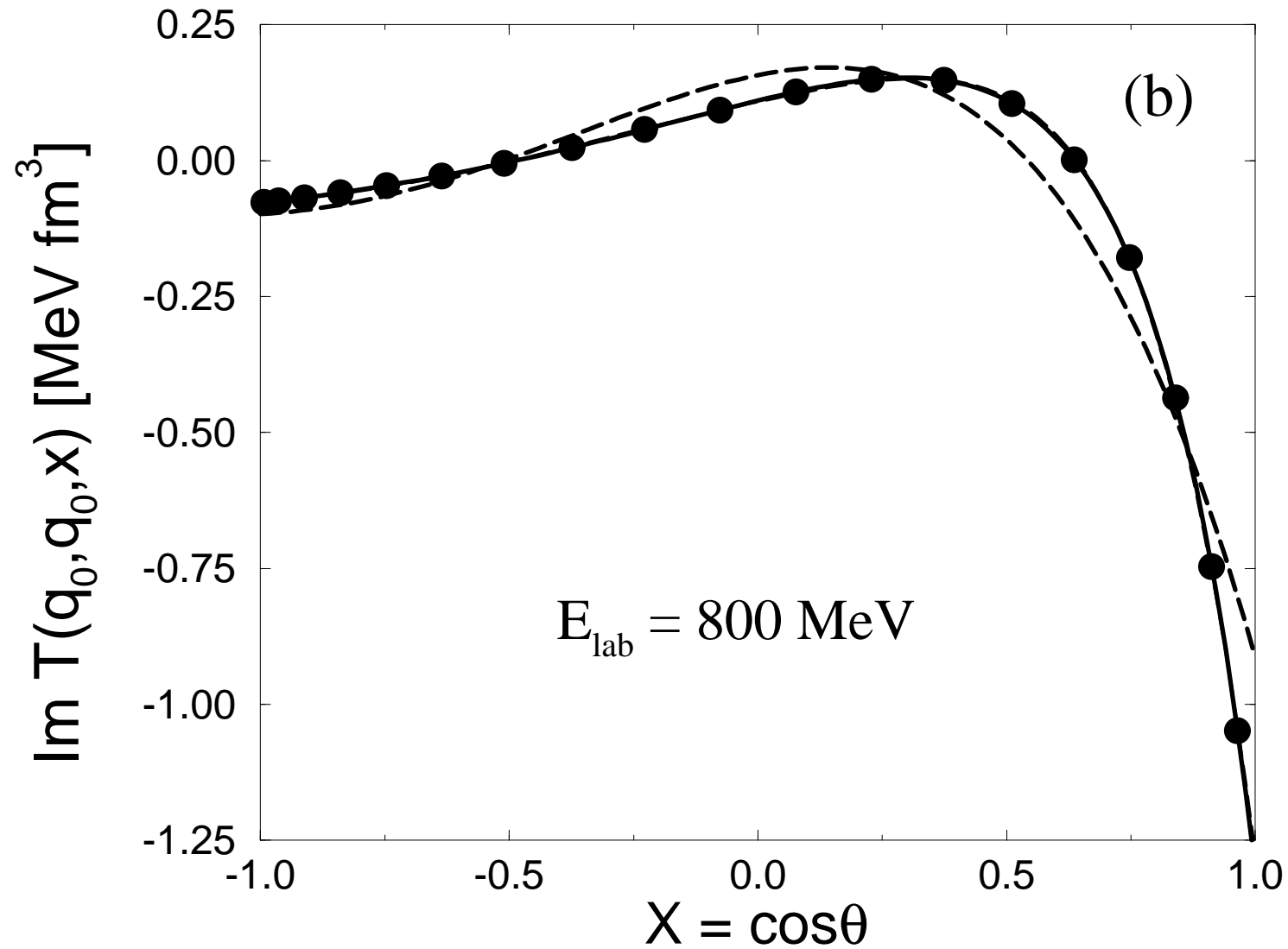


Fig. 2b



This figure "fig3.gif" is available in "gif" format from:

<http://arxiv.org/ps/nucl-th/9708017v1>

This figure "fig4.gif" is available in "gif" format from:

<http://arxiv.org/ps/nucl-th/9708017v1>

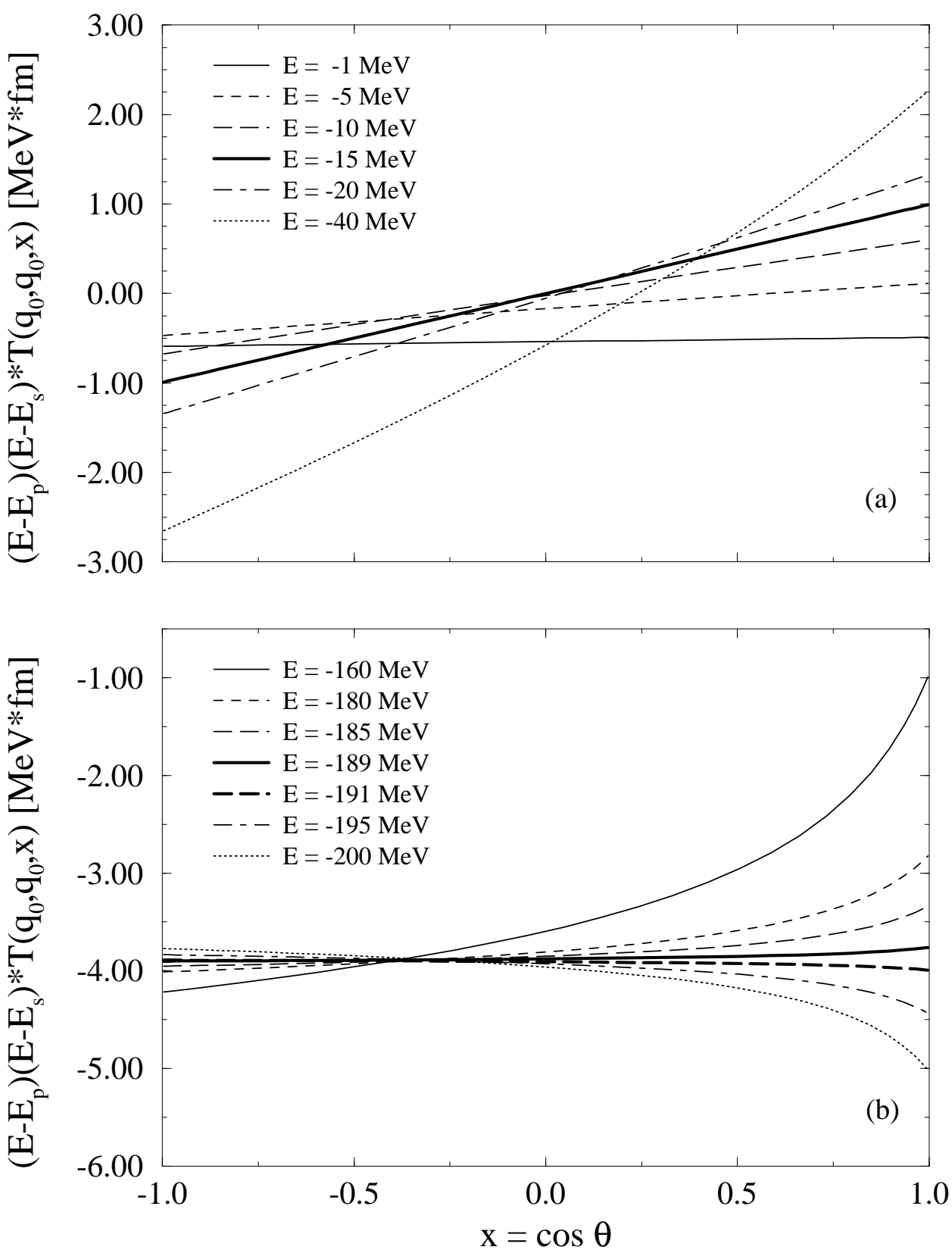
This figure "fig5.gif" is available in "gif" format from:

<http://arxiv.org/ps/nucl-th/9708017v1>

This figure "fig6.gif" is available in "gif" format from:

<http://arxiv.org/ps/nucl-th/9708017v1>

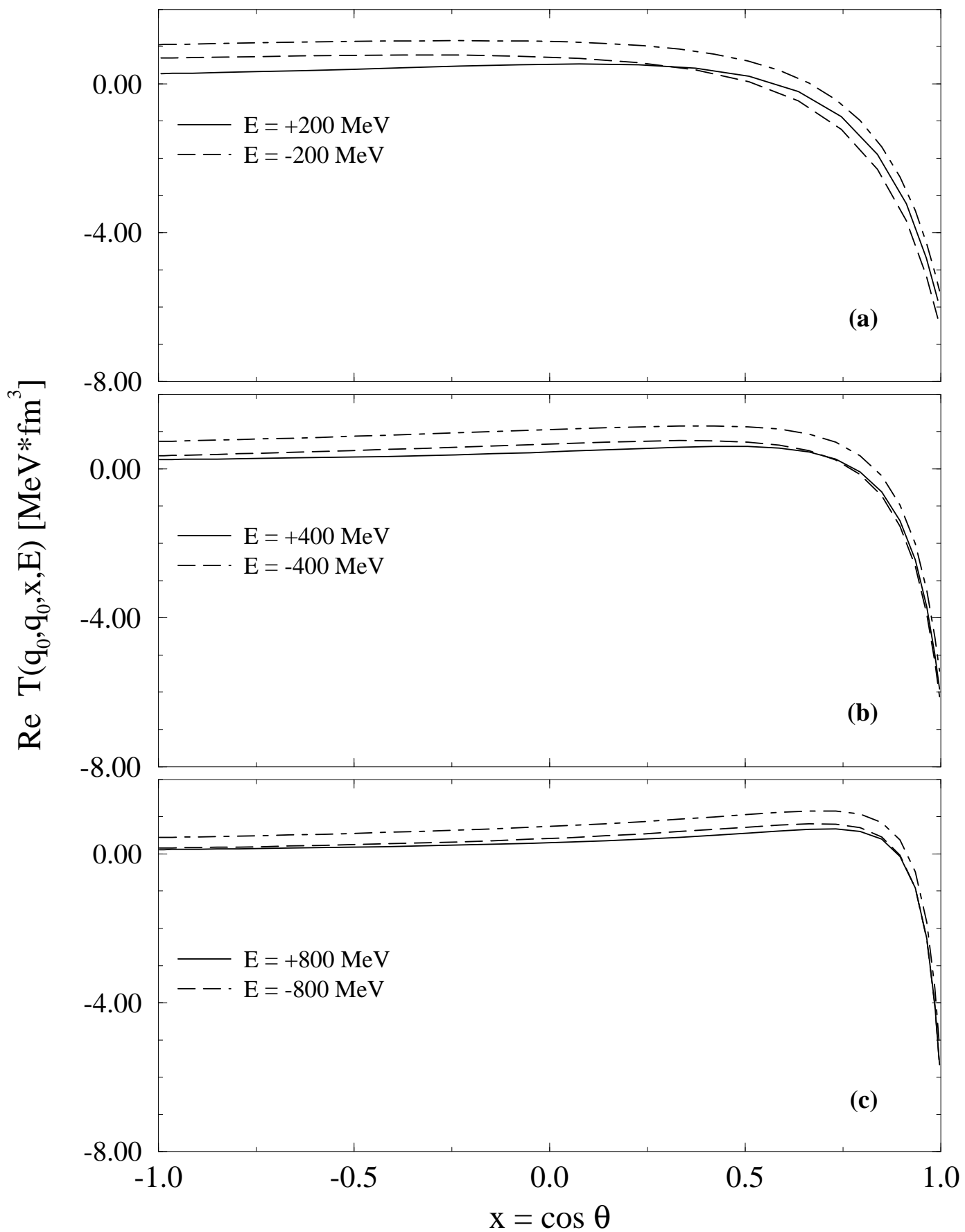
Fig. 7



This figure "fig8.gif" is available in "gif" format from:

<http://arxiv.org/ps/nucl-th/9708017v1>

Fig. 9



This figure "fig10.gif" is available in "gif" format from:

<http://arxiv.org/ps/nucl-th/9708017v1>

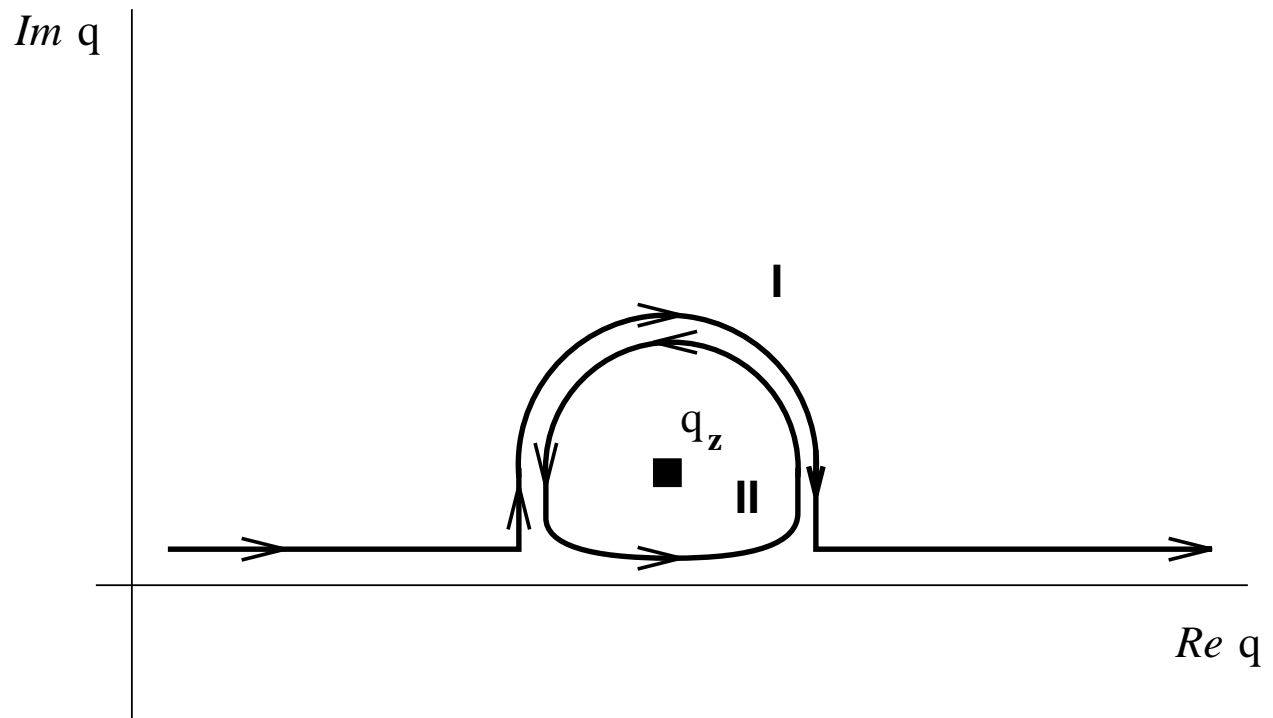


Fig. 11

Fig. 12

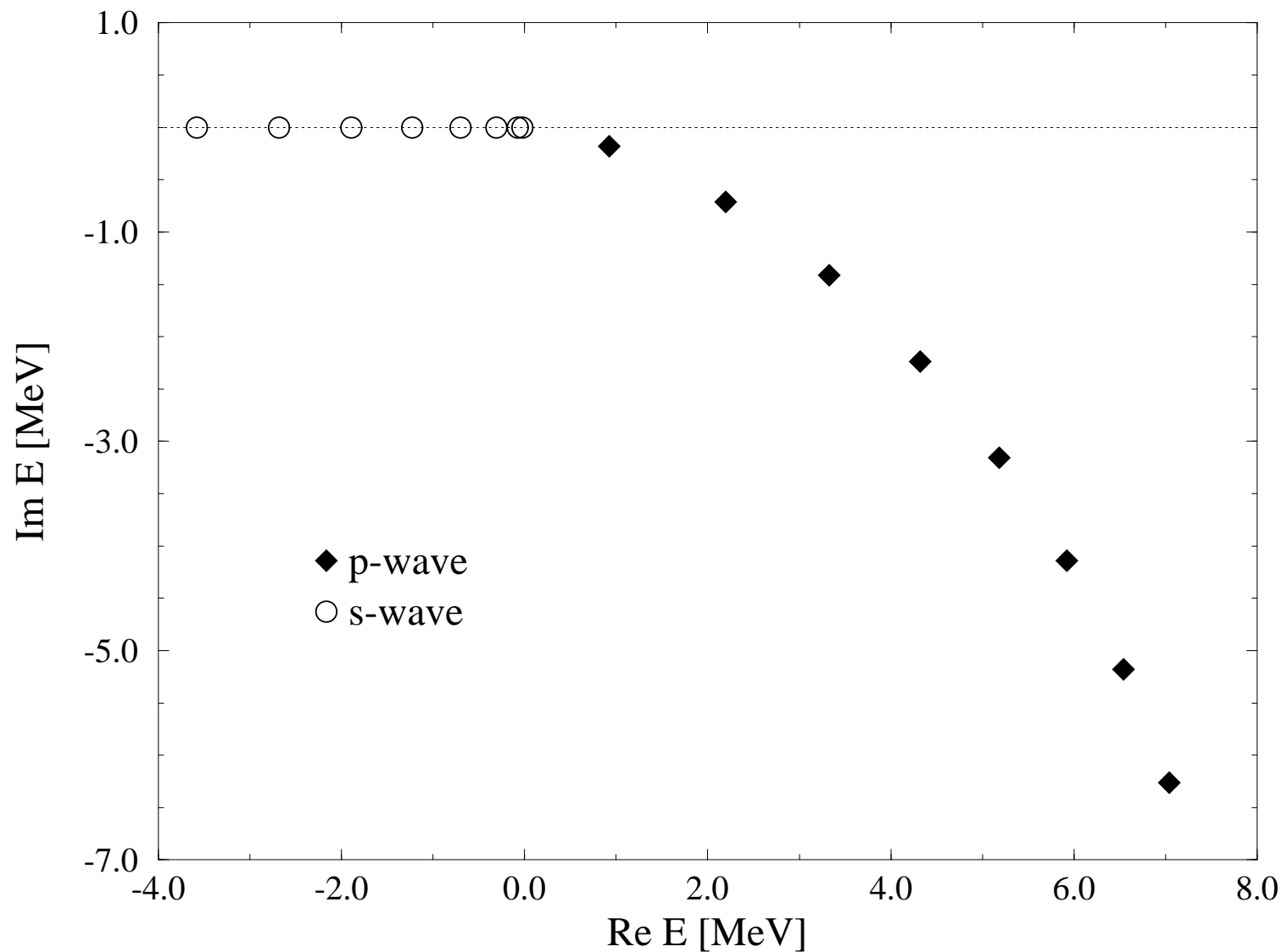


Fig. 13

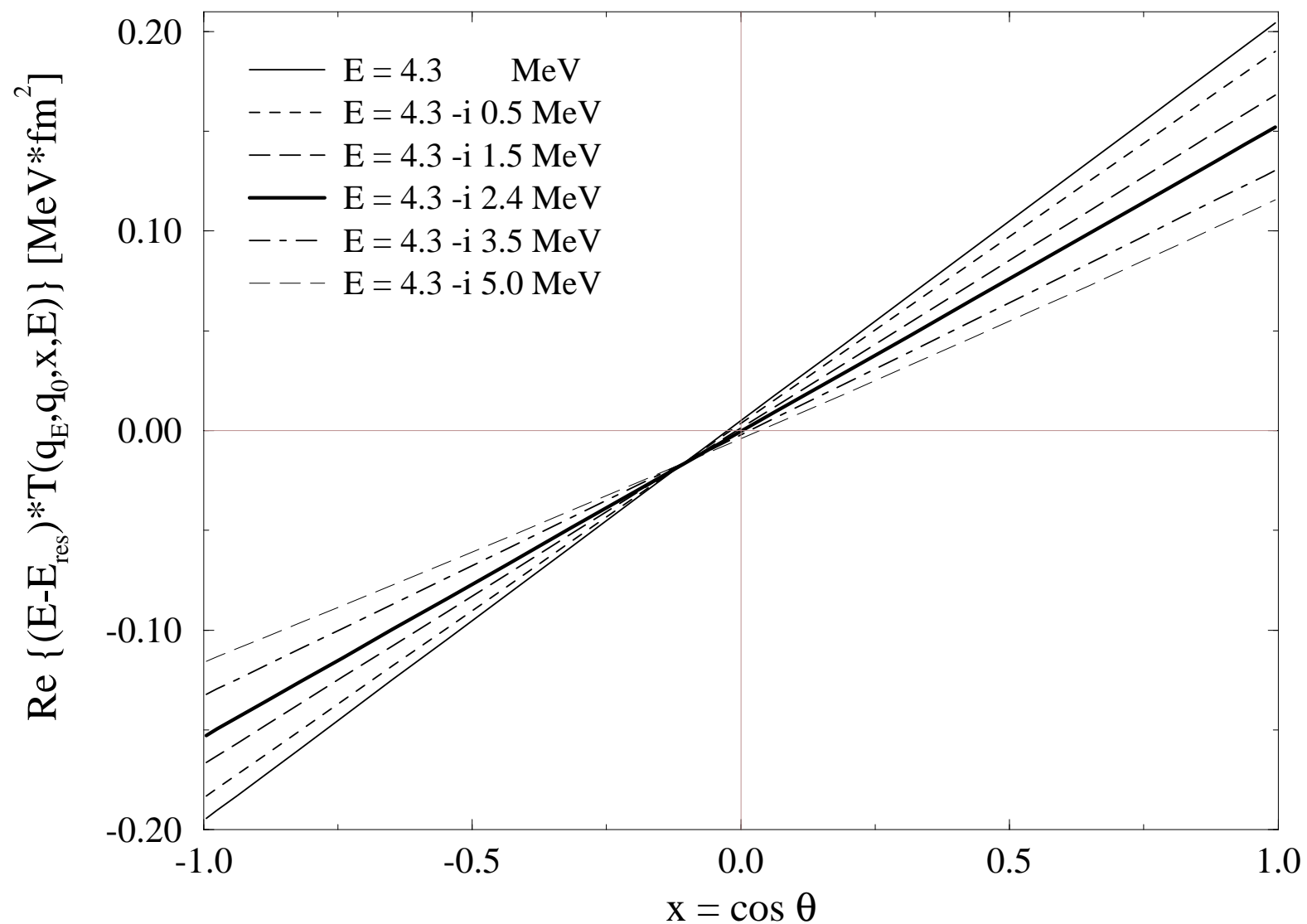


Fig. 14

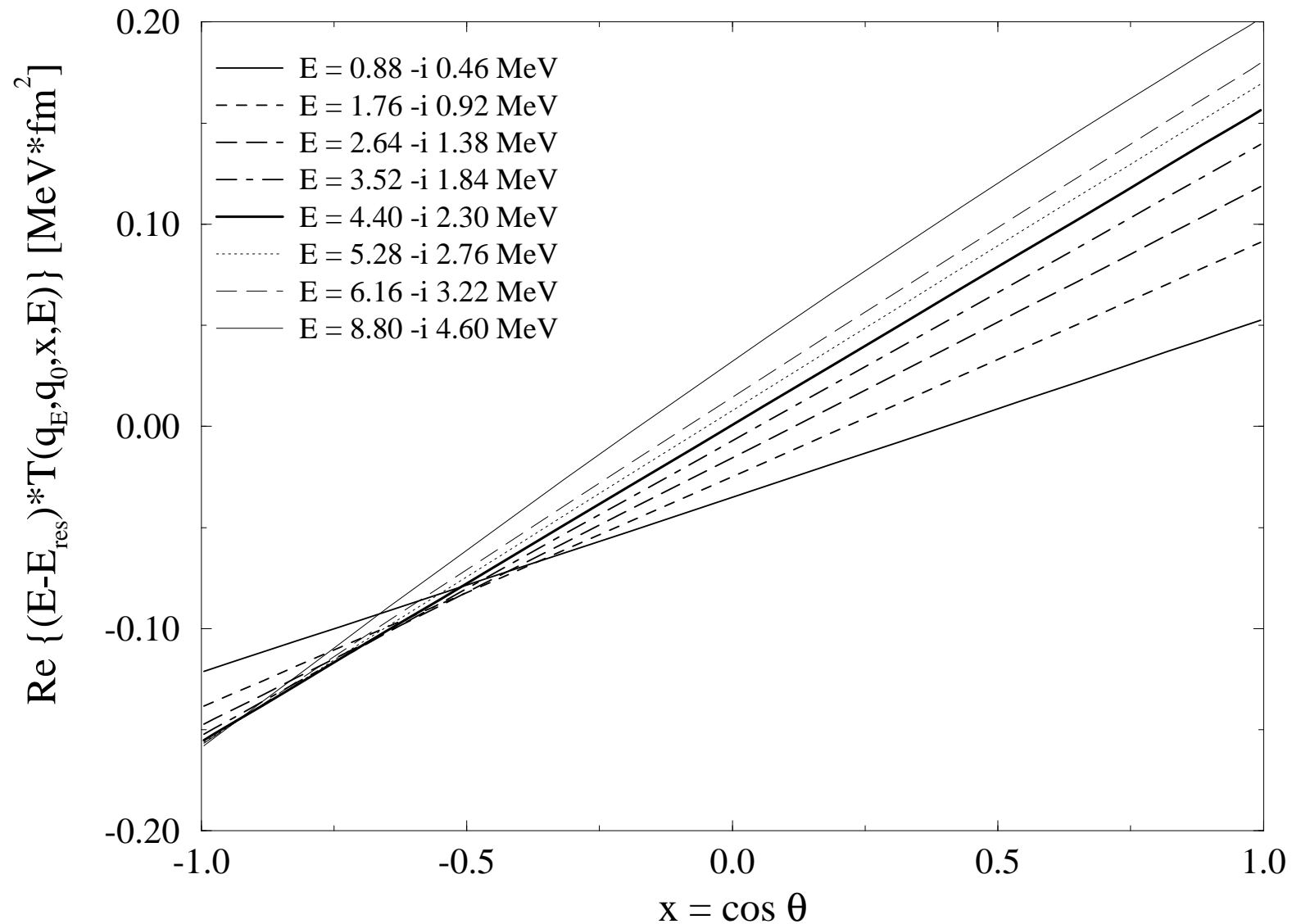


Fig. 15

